

1 **Response of onshore oceanic heat supply to yearly**
2 **changes in the Amundsen Sea icescape (Antarctica)**

3 **P. St-Laurent¹, S.E. Stammerjohn², T. Maksym³**

4 ¹Virginia Institute of Marine Science, William & Mary, Gloucester Point, VA

5 ²Institute of Arctic and Alpine Research (INSTAAR), University of Colorado, Boulder, CO

6 ³Applied Ocean Physics & Engineering, Woods Hole Oceanographic Institution, Woods Hole, MA

7 **Key Points:**

- 8 • Ice shelves such as Crosson and Thwaites have multiple viable sources of oceanic
9 heat helping to sustain their high melting rates
- 10 • The relative importance of these sources evolve in response to changes in icescape
11 such as the collapse of the Thwaites Glacier Tongue
- 12 • The fast-ice cover seaward of Pine Island Glacier does not mitigate its high melt-
13 ing rates and has remote impacts reaching up to Crosson

Abstract

The heat transfer between the warm oceanic water and the floating portion of the Antarctic ice sheet (the ice shelves) occurs in a dynamic environment with year-to-year changes in the distribution of icebergs and fast-ice (the ‘icescape’). Dramatic events such as the collapse of glacier tongues are apparent in satellite images but oceanographic observations are insufficient to capture the synoptic impact of such events on the supply of oceanic heat to ice shelves. This study uses a 3D numerical model and semi-idealized experiments to examine whether the current high melting rates of ice shelves in the Amundsen Sea could be mitigated by certain icescape configurations. Specifically, the experiments quantify the impacts on oceanic heat supply of presence/absence of the Thwaites Glacier Tongue, Bear Ridge Iceberg Chain, tabular iceberg B22, and fast-ice cover seaward of Pine Island Ice Shelf (PIS). The experiments reveal that future changes in the coastal icescape are unlikely to reverse the high ice shelf melting rates of the Amundsen Sea, and that icescape changes between 2011–2022 actually enhanced them slightly. Ice shelves such as Crosson and Thwaites are found to have multiple viable sources of oceanic heat whose relative importance may shift following icescape reconfigurations but the overall heat supply remains high. Similarly, the formation of a fast-ice cover seaward of PIS slows down the cavity circulation (by 7%) but does not reduce its heat supply.

Plain Language Summary

The Antarctic ice sheet is a gigantic volume of ice whose edges in certain locations are in direct contact with the ocean (‘ice shelves’). A warm oceanic water mass is causing the ice shelves to melt faster which accelerates the flow of ice from the Antarctic continent to the ocean. This contributes to a slow but steady rise in sea level that threatens the sustainability of coastal communities (where a large fraction of the world’s population lives). Preparing these communities for the future requires knowing how much sea level will rise and how fast. Our confidence in future sea level estimates is partly limited by the fact that ice shelf sizes and iceberg conditions change from one year to the next, leading to a complex, continuously evolving ice landscape (‘icescape’). We examined whether certain icescape configurations could hinder the circulation of warm water and limit how much heat comes in contact with the ice shelves. The computer simulations suggest that the ocean can rapidly adapt its pathways around the changing icescape in such a way that melting rates remain high. This result removes a layer of uncertainty from our estimates of future sea level rise.

1 Introduction

The floating portion of the Antarctic ice sheet, the ice shelves, exhibit some of their highest melting rates in the Amundsen Sea (Rignot et al., 2019) and have the potential to contribute to global sea level rise substantially over the next century (e.g., Joughin et al., 2021). The connection between the high melting rates and the presence of a warm oceanic water mass (modified Circumpolar Deep Water, mCDW) has been established for some time (e.g., Pritchard et al., 2012) but this heat transfer from the ocean to ice shelves occurs in a dynamic environment. For example, the seaward extent of Thwaites Ice Shelf (TIS, Fig. 1) varied by ~ 100 km over the years to periodically form the Thwaites Glacier Tongue (TGT; MacGregor et al., 2012). This mass of floating glacial ice ebbed and flowed following glacier acceleration/deceleration (e.g., Miles et al., 2020) and with the shedding of icebergs (‘calving’). In particular, the large tabular iceberg B22, that calved from Thwaites in 2002 (Stammerjohn et al., 2015), remained in the eastern Amundsen Sea until 2023. Its large size (82×44 km), combined with the proximity of the coast and of numerous smaller icebergs, contributed to heavy sea ice conditions between 107°W and 110°W during this period (Fig. 1).

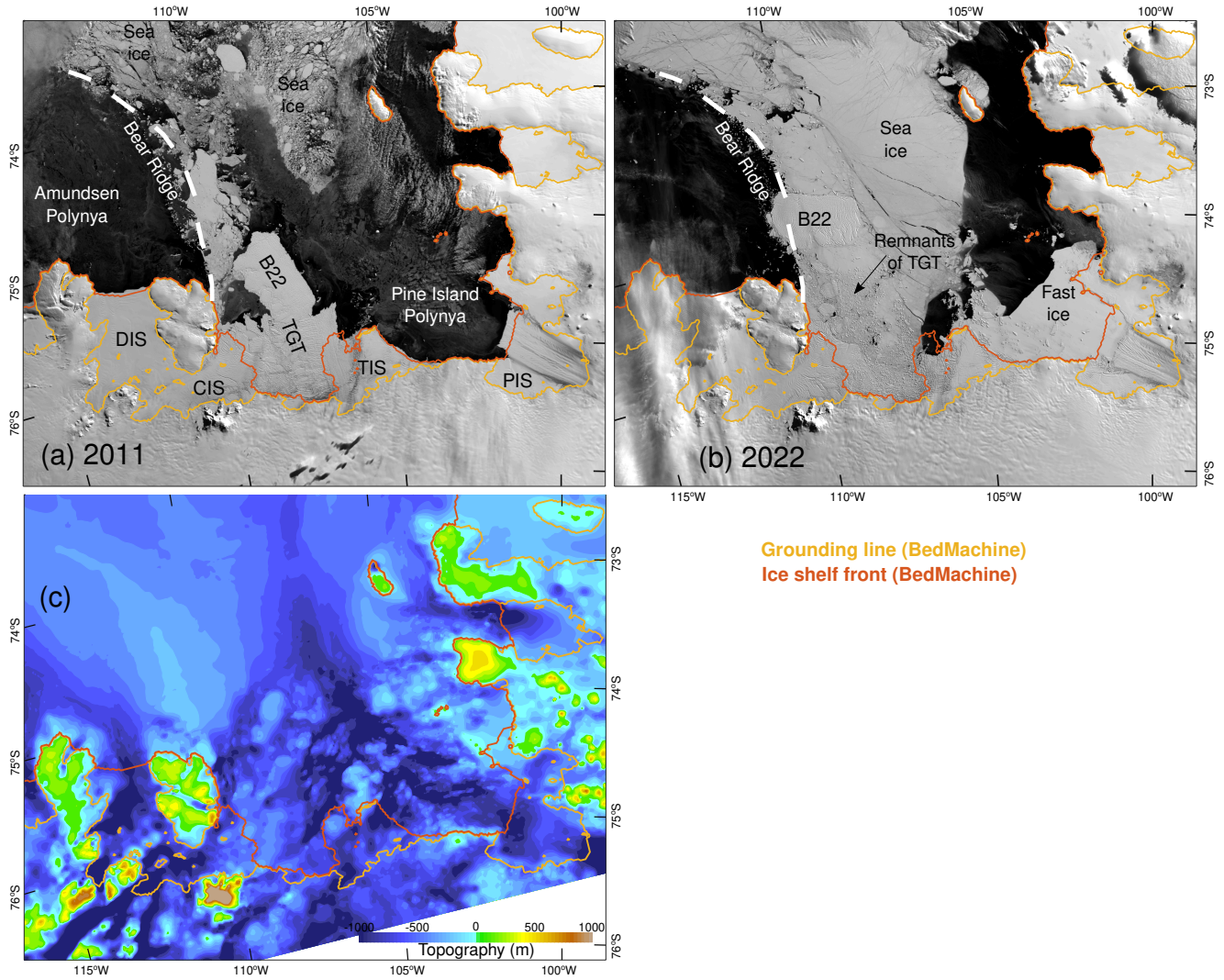


Figure 1. Contrast between two very different ‘icescape’ configurations in the eastern Amundsen Sea embayment. (a) Thwaites Glacier Tongue (TGT) at its maximum extent (Scambos et al., 2022, 9 March 2011). B22 is a tabular iceberg joined to the TGT on this date. (b) Complete breakup of the TGT into small individual icebergs, with a fast-ice cover between Thwaites Ice Shelf (TIS) and Pine Island Ice Shelf (PIS; 13 March 2022). Icebergs and ice shelves are distinguished from sea ice or fast-ice by their corrugated appearance. The dashed line represents Bear Ridge. DIS: Dotson Ice Shelf, CIS: Crosson Ice Shelf. (c) Topography of the study area. The grounding line and ice shelf front are from Morlighem (2020).

63 Another feature contributing to the regional ‘icescape’ is Bear Ridge, a shallow (\sim
 64 300 m deep) ridge extending seaward along 110°W from Bear Peninsula (Fig. 1). Icebergs
 65 become grounded along the ~ 150 km-long ridge to form an ‘iceberg chain’ (Macdonald
 66 et al., 2023; Mazur et al., 2019; Nakayama et al., 2014; Bett et al., 2020) which we re-
 67 fer to as the Bear Ridge Iceberg Chain (BRIC). Fast-ice forms between the grounded ice-
 68 bergs so that sea ice is unable to drift westward with the dominant winds, allowing the
 69 formation of the Amundsen Sea Polynya (ASP; Fig. 1a). The BRIC and the ASP are
 70 apparent every year in passive microwave-derived sea ice concentrations for 2006–2022
 71 (Comiso, 2017) and in visible satellite images for 2001–2022 (Scambos et al., 2022), sug-
 72 gesting these are permanent features of the Amundsen Sea. The area between TIS and
 73 Pine Island Ice Shelf (PIS) can also exhibit an extensive (~ 75 km-wide) fast-ice cover
 74 in some but not all years (it was present in eight out of 22 years between 2001–2022 (Scambos
 75 et al. (2022); see also Fig. 1b). At times, this fast-ice cover has remained in place for up
 76 to three years at a time (2004–2006) and therefore is not merely a seasonal feature.

77 These interannual variations in the Amundsen icescape have the potential to al-
 78 ter the supply of oceanic heat to ice shelves greatly. In contrast to the relatively mobile
 79 sea ice, fast-ice and ice shelves nearly completely shield the ocean from mechanical and
 80 thermodynamical exchanges with the atmosphere. The coastal oceanic circulation of the
 81 Amundsen is sensitive to this mechanical stress (Yang et al., 2022; Zheng et al., 2022;
 82 Kim et al., 2021) and is thus expected to change in response to the formation/collapse
 83 of the TGT (or of the fast-ice near PIS). For example, Dotto et al. (2022) report an up-
 84 lift of isotherms under TIS in response to the formation of the PIS fast-ice around 2021.
 85 Also, ice shelf fronts (and the icebergs shed from them) have very thick drafts $O(300\text{ m})$,
 86 i.e. comparable to the pycnocline depth in the Amundsen Sea (e.g., Jacobs et al., 2012).
 87 When the TGT grows over the years, the surface oceanic circulation is forced to be re-
 88 directed around the growing obstacle, and away from the coast and the grounding zones.
 89 Fast-ice, glacial ice tongues, and grounded icebergs can also alter sea ice production sim-
 90 ply by displacing polynyas or creating new ones. In turn, this production can affect the
 91 thermocline depth, a key parameter in determining basal melt rates (De Rydt et al., 2014).

92 Given these considerations, we raise the question: could the high ice shelf melting
 93 rates currently observed in the Amundsen Sea be mitigated by certain icescape config-
 94 urations? This question is the primary motivation for the present study, which aims at
 95 evaluating how regional changes in icescape might impact oceanic heat pathways and
 96 basal melt rates (e.g., Cougnon et al. (2017), in the context of the Mertz Glacier Tongue).
 97 Specifically, the study focuses on abrupt, year-to-year changes such as the collapse of the
 98 TGT between 2011 and 2013, or the periodic formation of the fast-ice cover near PIS.
 99 The study complements earlier efforts focused on the impact of iceberg chains and their
 100 melt on the Amundsen hydrography (Nakayama et al., 2014; Bett et al., 2020). Another
 101 question related to the Amundsen’s icescape is how freely mCDW circulates under large
 102 tabular icebergs such as B22. From a dynamical perspective, an isolated tabular iceberg
 103 can be conceptualized as an inverted seamount. Depending on the vertical stratification,
 104 iceberg keel, and background flow, the presence of the iceberg can lead to partial/total
 105 blocking of the oceanic flow (Taylor columns; e.g., Ou, 1991). Here, partial/total block-
 106 ing refers to the fluid from upstream being able to occupy a portion of the area under
 107 the iceberg (partial) or none of it (total blocking). Although iceberg melt does not con-
 108 tribute to sea level rise, whether blocking occurs or not under a tabular iceberg can dras-
 109 tically change its contribution to regional freshwater fluxes.

110 The study is structured as follows. The experimental plan used to highlight im-
 111 pacts of changes in icescape is described in the next section. It includes an evaluation
 112 of the numerical model used for these experiments against historical cryospheric/oceanic
 113 observations. The analyses presented in the subsequent sections focus on heat delivery
 114 to the ice shelves, the dynamical impact of fast-ice, polynya dynamics, and heat supply

115 under tabular icebergs. A discussion of these results in the context of the literature and
 116 of ongoing sea level rise conclude the study.

117 2 Methods

118 The study examines the impact of changes in icescape configuration on the oceanic
 119 heat supply to the ice shelves of the eastern Amundsen Sea. A set of numerical exper-
 120 iments is used to represent two contrasted configurations of the Thwaites Glacier Tongue
 121 (TGT; year 2011 versus 2022) while preserving all other components of the simulation
 122 the same to facilitate the interpretation. Additional experiments are used to highlight
 123 the role of the Bear Ridge Iceberg Chain (BRIC) and that of the fast-ice cover near PIS.
 124 Note that although drifting sea ice could be considered a component of the regional ‘icescape’,
 125 we interpret icescape as the collection of fast-ice, ice shelves, and icebergs.

126 2.1 Numerical model

127 The numerical model is an implementation of the Regional Ocean Modeling Sys-
 128 tem (ROMS, Shchepetkin & McWilliams, 2005) for the Amundsen Sea ($\sim 90\text{--}140^\circ\text{W}$, $\sim 68\text{--}$
 129 76°S ; St-Laurent, 2023). The computational grid has a uniform mesh size of 1.5 km in
 130 the horizontal plane and 20 topography-following levels. For comparison, the first baro-
 131 clinic Rossby radius of deformation is ~ 4.4 km on the continental shelf. The model in-
 132 cludes a dynamic and thermodynamic sea ice module (Budgell, 2005) and thermodynamic
 133 ice shelves (Dinniman et al., 2011). The implementation is similar to that of St-Laurent
 134 et al. (2017) but benefits from improvements: a slightly larger regional domain, recent
 135 ROMS codebase (6 April 2020), topographic refinements (Dorschel et al., 2022; Jordan
 136 et al., 2020; Morlighem, 2020), 3-hourly meteorological forcing from ERA5 (Hersbach
 137 et al., 2020), tidal forcing for 10 constituents (Padman et al., 2002), and 5 km-resolution
 138 oceanic boundary conditions from Dinniman et al. (2020).

139 The vertical coordinate of the model imposes restrictions on how abruptly topog-
 140 raphy is allowed to change from one horizontal grid cell to the next (e.g., Shchepetkin
 141 & McWilliams, 2003). This is addressed by numerically smoothing the seabed topog-
 142 raphy as well as the ice shelf (and iceberg) drafts (an approximation since in reality ice
 143 shelf fronts and recently calved icebergs are assumed to have vertical edges correspond-
 144 ing to very steep slopes). In this model implementation, ice shelf fronts and iceberg edges
 145 are allowed a slope of 0.08 which corresponds to a vertical change of 120 m between two
 146 neighboring grid cells. Therefore, the transition between a 300 m-thick iceberg draft and
 147 open water would occur over ~ 3 grid cells. The physical consequence of this approx-
 148 imation is that the real potential vorticity gradient is underestimated by the model and
 149 that horizontal exchanges across this gradient could be overestimated. This is in con-
 150 trast to geopotential-coordinate models that allow for arbitrarily-steep slopes while ex-
 151 perencing other well-documented limitations (e.g., Gwyther et al., 2020).

152 2.2 Experimental plan

153 The numerical experiments of the study share the same initial condition (of 1 Jan-
 154 uary 2010) taken from a realistic hindcast of 2006–2022 with a time-invariant icescape
 155 representative of year 2010 (St-Laurent, 2023). The January 2010 initial condition is mod-
 156 ified to simulate four different icescapes mimicking conditions observed over the past 20 years
 157 (see below). Satellite images (Scambos et al., 2022) indicate that such changes in icescape,
 158 like the break-up of the TGT or of the PIS fast-ice cover, often occur over periods of a
 159 few months to a year. The experiments thus have a duration of two years (1 Jan. 2010
 160 to 31 Dec. 2011) where the first year (2010) is considered a “spin-up” allowing the ocean
 161 and sea ice to adjust themselves to the new icescape. For reference, the ‘flushing timescale’
 162 of an Amundsen ice shelf cavity, computed as its volume divided by the volume of wa-

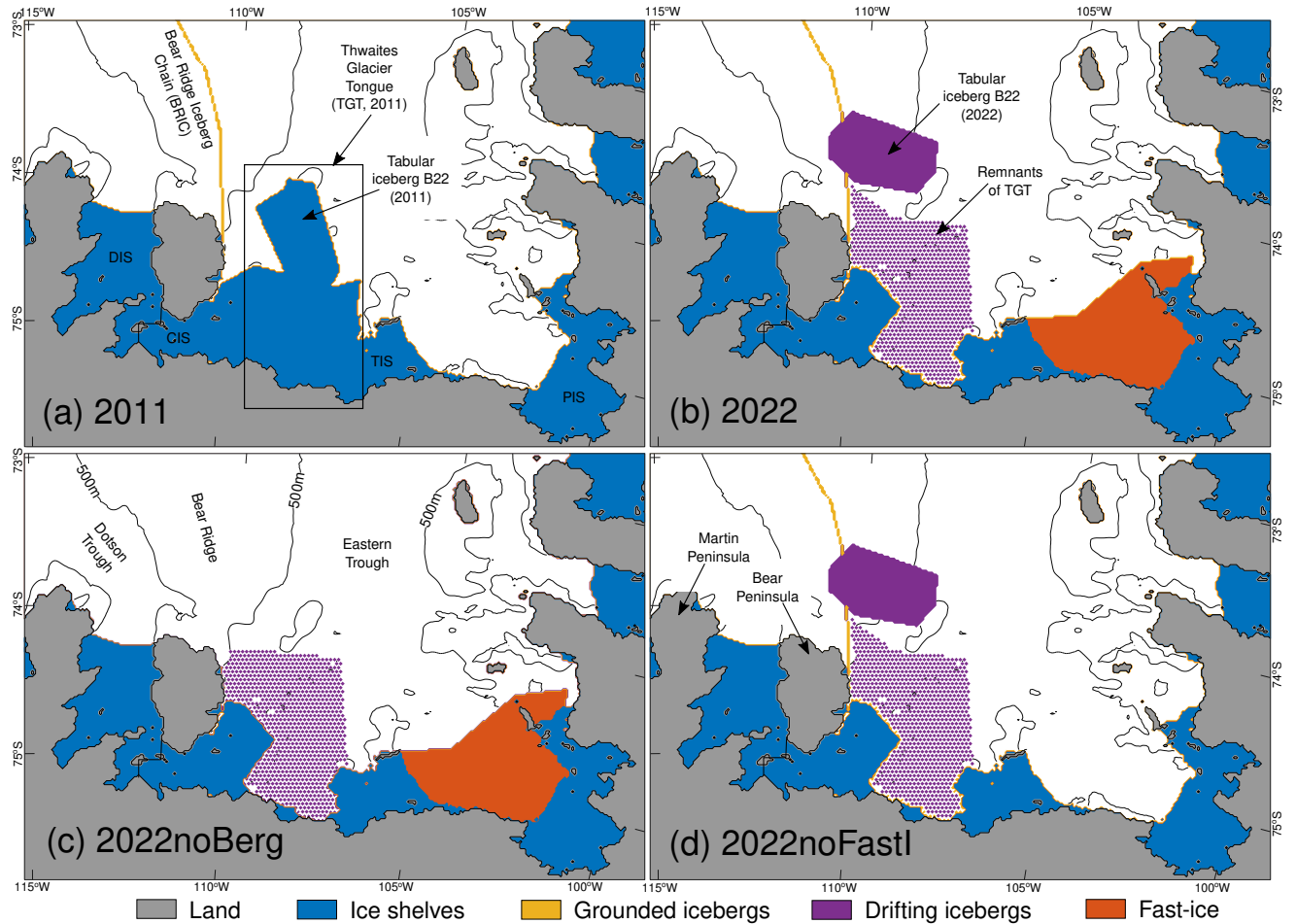


Figure 2. Geometry of the model experiments. (a) Year 2011, with key ice shelves labeled, (b) year 2022, (c) year 2022 without tabular iceberg B22 or the iceberg chain (2022noBerg), (d) year 2022 without fast-ice (2022noFastI). The key oceanographic and geographic features are highlighted in (c) and (d), respectively. The assumed boundary between Dotson Ice Shelf (DIS) and Crosson Ice Shelf (CIS) is represented in (a) and loosely based on Rignot et al. (2013). TIS: Thwaites Ice Shelf, PIS: Pine Island Ice Shelf.

163 ter circulating through it (~ 1 Sv, e.g., Jourdain et al., 2017) is $O(1$ month) and thus
 164 ice shelves adjust rapidly to changes in ambient conditions. All the analyses presented
 165 in the study are based on the second year of the experiments (2011). The possibility that
 166 the results could be sensitive to the time period (2010–2011) is investigated in additional
 167 experiments (see §2.3).

168 All four experiments share the same meteorology and lateral boundary conditions
 169 (edges of model domain) of 2010–2011 (even when the icescape represents year 2022) so
 170 that differences among the experiments are solely due to the icescapes. *Experiment 2011*
 171 represents the TGT at its maximum extent (Figs. 1a,2a). For CIS and TIS, the ice shelf
 172 draft of BedMachine is extended seaward assuming a fixed draft of 300 m to mimic the
 173 2011 TGT. The BRIC, a chain of small individual icebergs grounded along Bear Ridge
 174 and interconnected with fast-ice, is represented in the model by a fixed surface obsta-
 175 cle with a thin draft of arbitrary value (0.1 m). While this value is thinner than typical
 176 fast ice, it allows the ocean to circulate unimpeded (as the real ocean does in between

177 the individual icebergs forming the BRIC) while at the same time preventing the west-
 178 ward drift of modeled sea ice (and thus allowing the formation of the Amundsen Sea Polynya;
 179 Fig. 1a). The TGT and the BRIC are represented in the model as ice shelves and have
 180 a fixed location and thickness over time. The ice shelves are assumed to be insulated from
 181 the atmosphere but they exchange heat and freshwater with the ocean based on local
 182 hydrodynamics and hydrographic conditions (Dinniman et al., 2011). In the case of the
 183 BRIC, these exchanges are very small given its small surface area (Figs. 2a) and the fact
 184 that near-surface temperatures remain close to freezing except during the short austral
 185 summer. There is no attempt at representing the regional freshwater input from icebergs
 186 (e.g., Bett et al., 2020) besides the TGT/BRIC parameterizations described above.

187 *Experiment 2022* represents a collapsed TGT with the outline of the CIS and TIS
 188 mimicking satellite images (Figs. 1b,2b). Tabular iceberg B22 is now detached from the
 189 TIS and positioned northwest of its 2011 location. It has an assumed draft of 300 m (which
 190 allows for an oceanic flow underneath) and we neglect its drift over the period of the ex-
 191 periment (2 years). The numerous small drifting icebergs occupying the original loca-
 192 tion of the TGT are represented by a regular mesh of individual model grid points with
 193 fixed locations and an assumed draft of 0.1 m (“remnant of TGT”; Figs. 1b,2b). As be-
 194 fore, the 0.1 m is an arbitrary value allowing for an unimpeded oceanic circulation while
 195 modifying the modeled sea ice drift. The regular mesh limits the drift of modeled sea
 196 ice without completely blocking it and, overall, forms seasonal sea ice distributions con-
 197 sistent with satellite images (see §2.5). Year 2022 also exhibits an extensive and smooth
 198 region of ice cover between TIS and PIS (Figs. 1b,2b). This fast-ice is represented as an
 199 extension of TIS/PIS with an assumed draft of 0.1 m. The fast-ice prevents any mechan-
 200 ical forcing from winds and features a quadratic drag function of the ocean velocity at
 201 the ice/ocean interface. Although the fast-ice cover is allowed to exchange heat/freshwater
 202 with the ocean, its impact on the local hydrography is negligible compared to the thicker
 203 portions of the ice shelves that are positioned below the thermocline. Neither the fast-
 204 ice cover nor the remnant of the TGT are allowed to exchange fluxes with the atmosphere.

205 The purpose of *Experiment 2022noBerg* is to highlight the role of the BRIC and
 206 of tabular iceberg B22 by removing them from the 2022 icescape. Although satellite im-
 207 ages going back to 2001 suggest that the BRIC is a permanent feature, the experiment
 208 clarifies how much the local ocean circulation and sea ice patterns owe to the presence
 209 of the BRIC, and what they could look like if changing wind patterns were to transport
 210 icebergs away from Bear Ridge. The PIS fast-ice and the TGT remnants remain in place
 211 although the latter is cropped at the northern edge of Bear Peninsula to allow for a free
 212 sea ice drift. *Experiment 2022noFastI* is identical to Experiment 2022 except for the ab-
 213 sence of fast-ice in front of PIS so that its impact on the results can be evaluated. Note
 214 that this fast-ice gradually disappeared in the months following March 2022 (Scambos
 215 et al., 2022) and that 2022noFastI is representative of conditions in early 2023.

216 The four experiments above are designed so that pair-wise comparisons between
 217 them highlight the contribution of specific icescape changes. For example, experiments 2011
 218 and 2022noFastI both lack fast-ice in front of PIS, and the only thing distinguishing the
 219 two is the collapse of the TGT (Fig. 2a,d). By subtracting the basal melt rate of ex-
 220 periment 2011 from that of 2022noFastI, one obtains the impact of this collapse on basal
 221 melt. Similarly, subtracting 2022noFastI from experiment 2022 provides the impact of
 222 the fast-ice in front of PIS (Fig. 2b,d). Subtracting experiment 2022 from 2022noBerg
 223 provides the impact of a hypothetical disappearance of the BRIC (Fig. 2a,c).

224 2.3 Sensitivity experiments

225 The set of experiments described above does not address the possibility that the
 226 impacts of icescape changes could vary depending on background hydrographic condi-
 227 tions. Observations from the Amundsen Sea (Kim et al., 2021, their Fig. 8b) indicate that

228 2010–2011 was a relatively warm period followed by substantially cooler conditions in
 229 2014–2015. To test the robustness of our conclusions regarding the impacts of icescape
 230 changes, we conduct four additional experiments identical to the ones described above
 231 except that: (1) the initial condition corresponds to 1 January 2014, and (2) the mete-
 232 orology and lateral boundary conditions (edges of model domain) are for 2014–2015. This
 233 initial condition is taken from the same 2006–2022 hindcast (St-Laurent, 2023) that in-
 234 cludes the warm/cool contrast (see Fig. S1). The four additional experiments are inden-
 235 tified with the suffix ‘cold’ to distinguish them from their 2010–2011 counterpart. For
 236 example, experiments ‘2011’ and ‘2011_cold’ share the same icescape configuration but
 237 differ in their hydrology/meteorology, and so on for the pairs ‘2022’ and ‘2022_cold’, ‘2022noBerg’
 238 and ‘2022noBerg_cold’, ‘2022noFastI’ and ‘2022noFastI_cold’.

239 An additional experiment (*2011FastI*, combining the ice shelf configuration of ex-
 240 periment 2011 and fast-ice in front of PIS) is conducted to evaluate the additivity of the
 241 oceanographic impacts of icescape changes between 2011 and 2022 (the latter including
 242 the TGT collapse and fast-ice in front of PIS; Fig. 2). Mathematical additivity would
 243 correspond to $impacts(TGT\ collapse + fast\ ice) = impacts(TGT\ collapse) + impacts(fast\ ice)$.
 244 The additivity is tested by comparing results from experiments (2022 – 2011) against
 245 those of (2022noFastI – 2011) + (2011FastI – 2011). Any mismatch (nonlinearity) is in-
 246 terpreted as physical interactions arising when all icescape changes are present simul-
 247 taneously.

248 2.4 Analyses: Horizontal oceanic fluxes of volume and heat

249 The model saves the daily-averaged 3D horizontal volumetric flux \mathbf{Q}_{horiz} and po-
 250 tential temperature θ which are used to compute *a posteriori* the horizontal fluxes en-
 251 tering/leaving the ice shelf cavities. Note that the diurnal tidal constituents are the dom-
 252 inant ones in the Amundsen Sea and thus the daily average effectively filters tidal cy-
 253 cles (which are already fairly weak on the inner continental shelf; see Jourdain et al. (2019)).
 254 The heat flux is computed as $\rho_0 c_p \mathbf{Q}_{horiz} (\theta - \theta_0)$ where $\rho_0 = 1028\text{ kg m}^{-3}$ is a refer-
 255 ence value for seawater density, $c_p = 4 \times 10^3\text{ J (kg K)}^{-1}$ the specific heat, and $\theta_0 =$
 256 -1.85°C is a constant representative of the surface freezing temperature of seawater and
 257 of the ‘Winter Water’ layer occupying the upper $\sim 300\text{ m}$ of the water column (e.g., Randall-
 258 Goodwin et al., 2015). This choice of θ_0 ensures that only mCDW contributes to the heat
 259 flux (e.g., Jourdain et al., 2017).

260 For a given section such as the front of an ice shelf and for a given day of year 2011,
 261 the volume and heat fluxes perpendicular to the section are grouped into ‘entering’ or
 262 ‘leaving’ the ice shelf depending on the sign of the volumetric flux, and then they are av-
 263 eraged over the year 2011. The resulting decomposition reflects vertical and/or lateral
 264 variations in the horizontal flow perpendicular to the ice shelf front. The difference be-
 265 tween the heat flux that enters or leaves an ice shelf cavity (i.e., the net heat flux) matches
 266 the ice shelf’s 2011-averaged basal melt except for small variations in the cavity’s heat
 267 content. Two-dimensional maps of the horizontal heat flux are also constructed by av-
 268 eraging this flux over year 2011 followed by a vertical summation over the 20 vertical lev-
 269 els.

270 2.5 Model-data comparisons

271 Daily sea ice concentrations at 25 km resolution from the Special Sensor Microwave/Imager
 272 (SSM/I) with the bootstrap algorithm (Comiso, 2017) are used to evaluate the modeled
 273 sea ice. Monthly averages of daily modeled/SSM/I concentrations are computed around
 274 the first day of the months of 2011 and plotted side-by-side. The model simulates the
 275 key features of the seasonal cycle relatively well including the open water area in Feb.-
 276 Mar., the timing of polynya opening (Dec.) and that of sea ice growth (March; Fig. 3).
 277 Note the presence of three well-developed coastal polynyas in the January image (in both

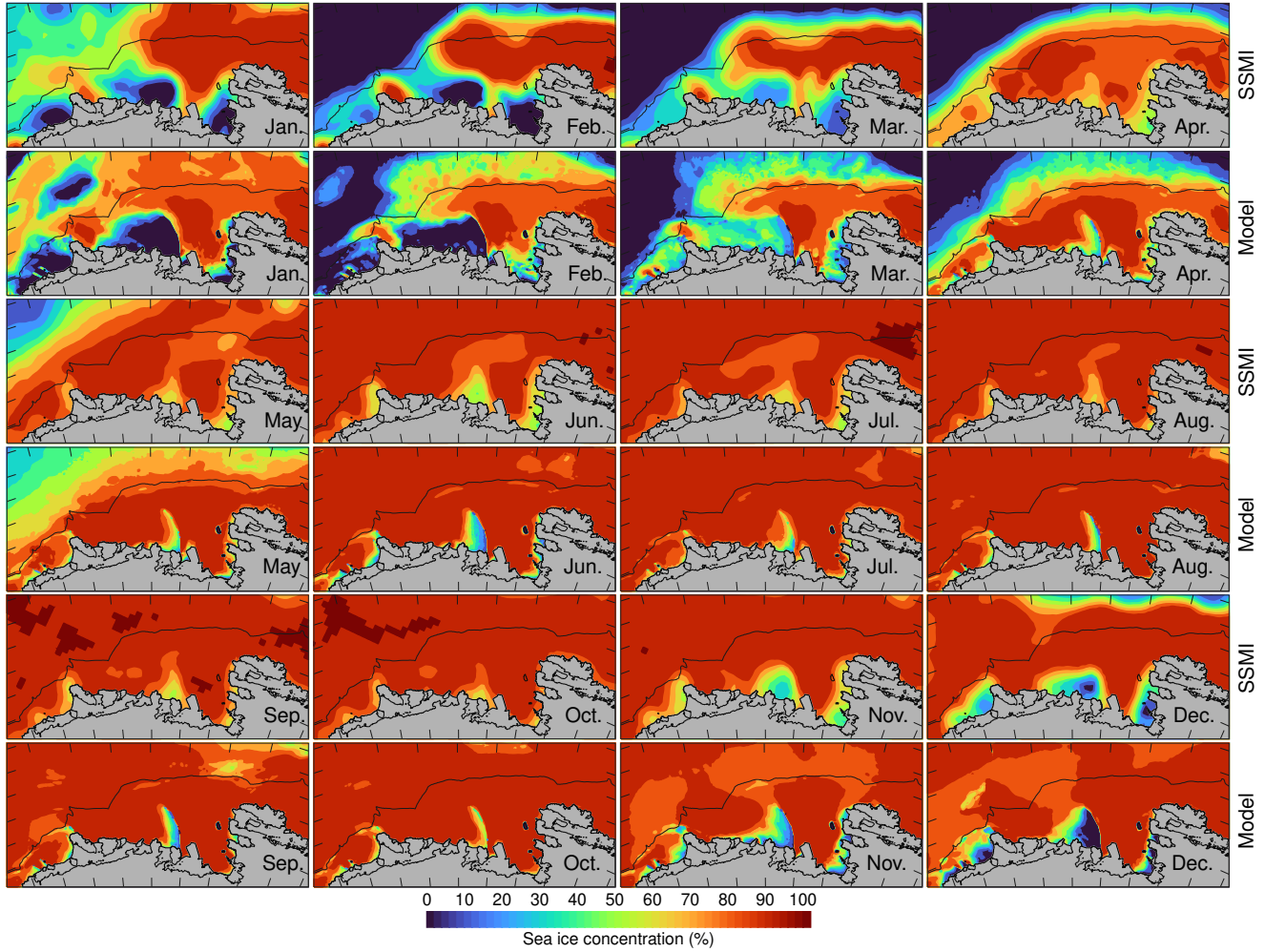


Figure 3. Comparison between sea ice concentration from satellite (SSM/I) and from experiment 2011. All fields are monthly averages centered around the first day of the month (1 Jan. 2011 to 1 Dec. 2011). The black horizontal line depicts the shelf break.

278 model and satellite): one next to Getz Ice Shelf (west of Siple Island), the Amundsen
 279 Sea Polynya, and the Pine Island Polynya. Relatively minor model biases include a high
 280 concentration bias over the Pine Island Polynya in Jan./Mar., a ASP that extends slightly
 281 too far north and west in Dec.-Feb., and a high concentration bias at the northern edge
 282 of the model domain in Dec.

283 Oceanographic data comprising 65 vertical profiles from the Amundsen Sea Polynya
 284 International Research Expedition (ASPIRE) collected between 13 December 2010 and
 285 8 January 2011 (P. L. Yager et al., 2012, 2016) are used to evaluate the modeled tem-
 286 perature and salinity in the Dotson area. The spatial coverage ranges from the shelf break
 287 ($\sim 71.5^\circ\text{S}$) to the Dotson ice shelf front and from $\sim 119^\circ\text{W}$ to Bear Ridge. The model
 288 reproduces the characteristics of the Amundsen hydrography including the warm salty
 289 layer of mCDW at depth and the weak, quasi-linear haline stratification (see Fig. S4).
 290 Note that in the Amundsen Sea, salinity dictates the vertical density stratification and
 291 that sub-surface salinity and temperature both increase with depth (e.g., Jacobs et al.,
 292 2012). Relatively small model biases include a 0.3°C warm bias centered around 200 m
 293 depth (i.e. in the ‘Winter Water’ layer) and a bias of $+0.1$ salinity units in the same layer.

294 A set of 106 hydrographic profiles from the eastern portion of the Amundsen Sea
 295 (72–90°S, 100–110°W, cruise NBP09-01 of Jan. 2009 to Feb. 2009) is used to evaluate
 296 the modeled temperature and salinity of that area. The model results for this evalua-
 297 tion are taken from the 2006–2022 hindcast of St-Laurent (2023). The model biases in-
 298 clude a warm bias around 250 m depth reaching up to +0.5°C and a salty bias at a sim-
 299 ilar depth reaching up to +0.15 psu (Fig. S5). Note that this warm bias may originate
 300 from the high sea ice concentration bias noted earlier for the same area (which would
 301 in turn lead to insufficient winter ventilation of the upper 300 m) or from excessive ver-
 302 tical diffusivity. Biases in the rest of the water column are much smaller and amount to
 303 –0.25°C and –0.1 psu in the bottom layer (800 m depth).

304 Observational estimates of ice shelf basal melt rates representative of 2003–2008
 305 (Rignot et al., 2013) are used as a comparison point for the modeled results (Fig. S6).
 306 Although the time period and the icescape geometry are not a match for either of the
 307 2011/2022 model configurations, the comparison indicates a broad agreement in the spa-
 308 tial distribution of basal melt as well as in their order of magnitude.

309 3 Results

310 This section focuses on four topics where changes in icescape were found to have
 311 a substantial impact: heat delivery to the ice shelves, the dynamical impact of fast-ice,
 312 polynya dynamics, and heat supply under tabular icebergs. The results are further dis-
 313 cussed in the context of the literature and of ongoing sea level rise in the last section of
 314 the study.

315 3.1 Supply of oceanic heat to the ice shelves

316 Basal melt under the ice shelves is associated with cyclonic (i.e., clockwise) circula-
 317 tions of volume and oceanic heat under DIS, CIS, TIS and PIS (Fig. 4). The cyclonic
 318 circulations form a two-way flow at the front of the ice shelves (i.e., entering/leaving the
 319 ice shelf) and at the boundary between DIS and CIS. In all cases, the two-way flow is
 320 an order of magnitude larger than the net flow across the ice shelf front and is $O(1\text{ Sv})$
 321 for volume and $O(10\text{ TW})$ for heat (Table S1). In other words, the majority of the oceanic
 322 heat circulates in/out of the ice shelves without contributing to basal melt (e.g., Jour-
 323 dain et al., 2017).

324 A two-way flow at the ice shelf fronts remains in place in all four model experiments
 325 (Table S1) but the pathways of heat can change appreciably in response to changes in
 326 icescape. Northeast of Bear Peninsula, a number of gyres are apparent with their spa-
 327 tial extent and their center varying in response to the position of B22, which affects the
 328 heat flux arrows at the front of CIS (Fig. 4a,b). Specifically, the northward migration
 329 of B22 and the collapse of TGT lead to a $\approx 20\%$ weaker heat flux entering/leaving the
 330 front of CIS (compare experiments 2011 and 2022noFastI in Table S1). Between PIS and
 331 TIS, the presence of fast-ice leads to a weaker cyclonic gyre seaward of PIS and a 7%
 332 reduction in the volume flux of PIS (Fig. 4c,d, Table S1). For TIS, the presence of fast-
 333 ice to the east and the absence of TGT to the west in the 2022 icescape leads to a shift
 334 in the relative importance of the various inflows, with relatively more heat coming from
 335 the western side of TIS in 2022 than in 2011 (Fig. 4c,d). Specifically, the contribution
 336 from the segment west of 106.5°W increased from 24% in 2011 to 40% in the 2022 icescape
 337 following the collapse of the TGT.

338 The impact of these changes in heat pathways is reflected in the net heat flux (i.e.
 339 the sum of the two-way flow) across the ice shelf fronts and across the Dotson/Crosson
 340 boundary. In 2011, the net flux across the CIS front is very weak (0.03 TW exiting the
 341 ice shelf) and CIS entirely depends on a 0.40 TW flux of heat coming from DIS in or-
 342 der to maintain its basal melt of 34.1 Gt yr⁻¹ (Table 1). In the 2022 icescape, the heat

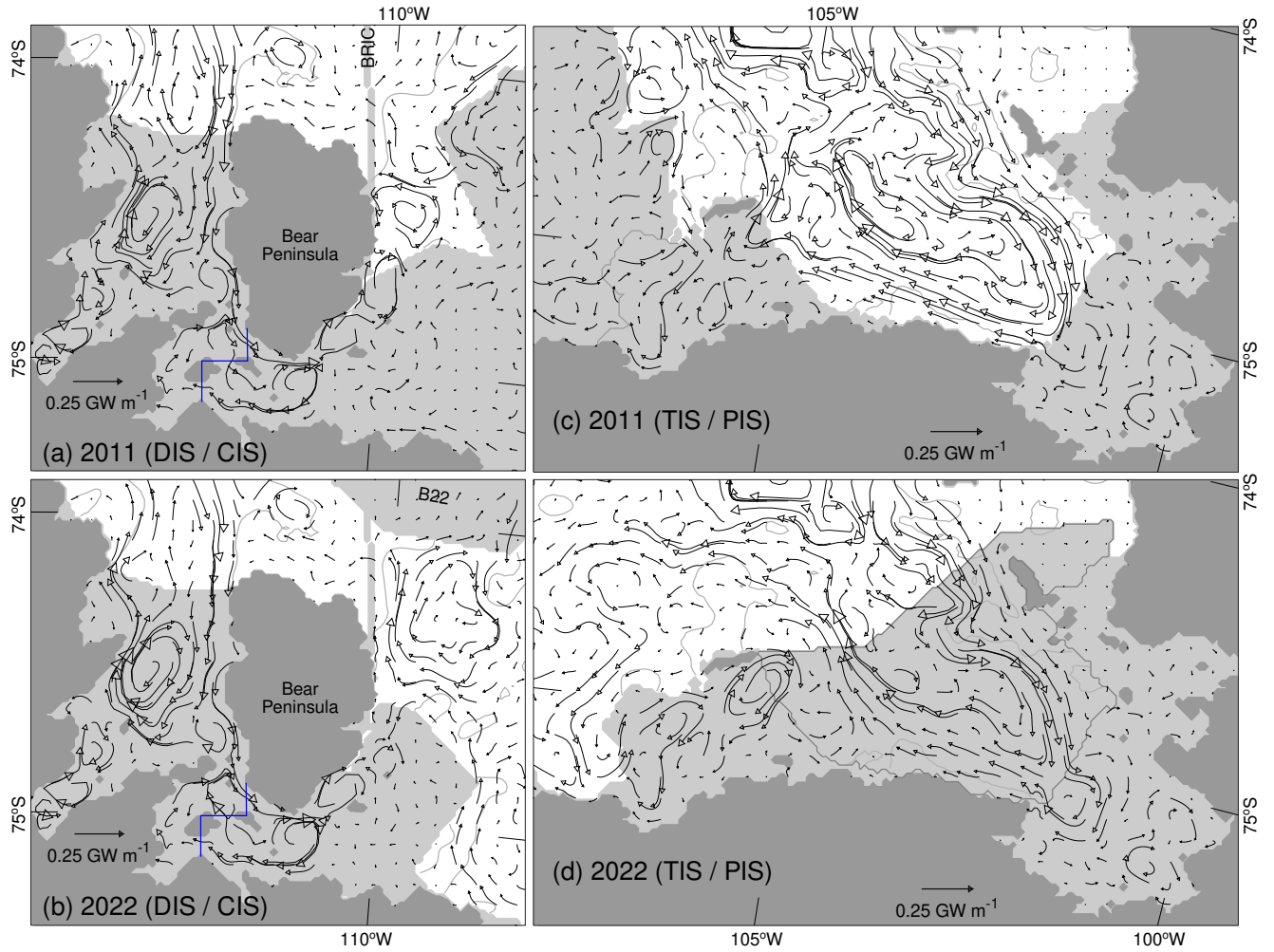


Figure 4. Horizontal oceanic heat flux in the vicinity of the ice shelves for two icescape configurations. (a) Heat flux near Dotson Ice Shelf (DIS) and Crosson Ice Shelf (CIS) in the 2011 and (b) 2022 configurations. (c,d) Same as a,b but for Thwaites Ice Shelf (TIS) and Pine Island Glacier Ice Shelf (PIS). The heat flux is vertically-integrated from the sea floor to the surface and averaged over the year 2011. Only one vector out of five is shown for clarity. The blue line is the assumed boundary between CIS and DIS. BRIC: Bear Ridge Iceberg Chain.

Table 1. Horizontal oceanic heat flux^a and ice shelf basal melt^b averaged over year 2011 in each icescape experiment

Horizontal oceanic heat flux (TW)					
Experiment	DIS	CIS	TIS	PIS	Do/Cr
2011	1.13	-0.03	0.75	0.93	-0.40
2022	0.89	0.40	0.99	1.01	-0.05
2022NoBerg	0.90	0.43	0.98	1.02	-0.02
2022NoFastI	1.01	0.23	0.85	0.97	-0.19
2011FastI	1.16	0.04	0.85	0.96	-0.36
Ice shelf basal melt (Gt yr ⁻¹)					
2011	68.6	34.1	69.7	89.6	
2022	76.6	42.2	83.2	96.3	
2022NoBerg	76.9	42.0	80.3	96.1	
2022NoFastI	72.7	38.3	71.2	91.6	
2011FastI	71.6	37.0	80.0	92.5	
Area (km ²)					
	5144	3479	2743	4750	
Volume (km ³)					
	2278	1211	1237	1418	

^aThe heat flux (see §2 for its equation and a definition of the acronyms) is integrated along the front of the ice shelf except for ‘Do/Cr’ where it is integrated along the boundary separating Dotson from Crosson; see Fig. 2a. The sign is positive when carrying heat into the ice shelf (and for ‘Do/Cr’, negative if flowing from Dotson to Crosson). See Table S1 for a decomposition of the flux into components entering/leaving the cavity.

^bThe ice shelf basal melt is horizontally integrated over the portion of the ice shelf common to all the experiments (with the area and cavity volume listed above).

1 Gt = 10¹² kg, 100 Gt yr⁻¹ ⇔ 1.0584 TW.

343 flux across the CIS front increases by 0.43 TW, allowing for a 24% increase in the basal
 344 melt of CIS. At the same time, the heat transported from DIS to CIS decreases by 0.35 TW,
 345 indicating that CIS’ heat source shifted between 2011 and 2022 from the DIS/CIS bound-
 346 ary to the front of CIS. The weakening of the exchanges between DIS and CIS in the 2022
 347 icescape more than compensates for a reduction in the heat flux at the DIS front, with
 348 the melt of DIS increasing by 11% between 2011 and 2022 (Table 1).

349 Turning to TIS and PIS, experiments 2022 and 2022noFastI indicate that the col-
 350 lapse of the TGT and the presence of a fast-ice cover both contribute to increased heat
 351 supply to these ice shelves (Table 1). In the case of TIS, the collapse of the TGT (and
 352 the corresponding changes in pathways) is responsible for 0.10 TW out of the 0.24 TW
 353 increase in heat flux between 2011 and 2022 with the remainder due to the formation
 354 of the fast-ice cover (about 0.10 TW based on experiments 2011 and 2011FastI) and a
 355 small nonlinearity (0.04 TW). It is notable that the fast-ice has a positive effect on the
 356 heat supply despite insulating the nearby ocean from the wind forcing and causing drag
 357 against the surface circulation (a topic further examined in §3.2). The basal melt of PIS
 358 and TIS reflects the change in heat fluxes, with increases of 7–19% between 2011 and
 359 2022. This increase in TIS’ melt is primarily due to the fast-ice cover (+10.3 Gt yr⁻¹
 360 based on experiments 2011 and 2011FastI) and to a lesser extent to the TGT’s collapse
 361 (+1.5 Gt yr⁻¹ based on experiments 2011 and 2022noFastI; Table 1). The fourth exper-
 362 iment, 2022noBerg, yields heat fluxes and basal melt rates that are very similar to ex-
 363 periment 2022 (Table 1). It indicates that on year-to-year timescales, the formation/disappearance
 364 of the BRIC standing on top of the shallow Bear Ridge would have a fairly limited im-

365 pact on the ice shelves’ heat supply despite the BRIC playing a critical role in sea ice
 366 distributions (see §3.3). (Note that Bett et al. (2020) reported a qualitatively similar out-
 367 come from a comparable experiment.)

368 The additivity of the response to icescape changes can be evaluated from exper-
 369 iments 2011, 2011FastI, 2022noFastI and 2022 (see §2.3). The basal melt rates are al-
 370 ways slightly higher when the icescape changes between 2011 and 2022 (TGT collapse
 371 and fast-ice) occur simultaneously by 11%, 12%, 13% and 27% for DIS, CIS, TIS, PIS,
 372 respectively (Table 1).

373 Repeating experiments 2011, 2022, 2022noBerg, and 2022noFastI in the cool oceanic
 374 conditions of 2015 leads to a general decrease in basal melt rates across icescape config-
 375 urations and across individual ice shelves (between 8 and 18 Gt yr⁻¹; compare Tables 1
 376 and S2). However, the impact of icescape changes on heat fluxes and basal melt rates,
 377 which corresponds to pair-wise differences between experiments having different icescape
 378 geometry but the same hydrography, is fairly similar under ‘warm’ or ‘cold’ conditions
 379 (see Fig. S7) since pair-wise differences are not affected by a \sim uniform offset in basal melt
 380 rates. The sign and the order of magnitude of the oceanographic response to icescape
 381 changes are similar for the hydrography of 2011 or 2015 (Fig. S7). For example, the ad-
 382 dition of PIS’s fast-ice (isolated from experiments 2022 and 2022NoFastI) increases the
 383 basal melt of TIS by +12.0 Gt yr⁻¹ in the warm conditions of 2011 and by +13.4 Gt yr⁻¹
 384 in the cool conditions of 2015 (Tables 1 and S2). Overall, the impact of icescape changes
 385 appears to be robust across hydrographic conditions.

386 **3.2 Fast-ice and its impact on the heat supply**

387 The presence of a fast-ice cover between TIS and PIS was shown to increase heat
 388 fluxes and basal melt in the eastern Amundsen Sea (§3.1). This result may reflect a ther-
 389 modynamic role played by fast-ice, e.g. where it insulates the ocean from the cold at-
 390 mosphere during the winter, or a dynamic role related to changes in the surface stress
 391 experienced by the ocean. Comparisons between experiments 2022noFastI and 2022 re-
 392 veal *lower* sub-surface temperatures seaward of PIS when fast-ice shields the ocean (not
 393 shown). Moreover, sea ice production in the eastern Amundsen Sea is either similar or
 394 slightly higher when the fast-ice is present (not shown). These results suggest a predom-
 395 inantly dynamical cause for the increase in basal melt. As noted in §3.1, the area west
 396 of PIS features a vigorous cyclonic circulation (gyre) corresponding to a local depression
 397 in the sea surface (Fig. 5a; see also Thurnherr et al. (2014) for direct observations of the
 398 gyre). The introduction of the fast-ice cover shields the ocean from the wind forcing and
 399 causes an appreciable slow down of the cyclonic gyre; the deceleration amounts to a flat-
 400 tening of the sea surface by up to 5 cm at the gyre’s center (Fig. 5b).

401 In absence of the fast-ice cover, the baroclinic structure of the cyclonic gyre cor-
 402 responds to a dome with elevated isopycnals/isotherms at the center and depressed isopy-
 403 cnals/isotherms at the periphery (Fig. 5c, as expected for horizontal velocity profiles weak-
 404 ening with depth). When the fast-ice cover is introduced, the dome flattens and the pe-
 405 ripheral isotherms are raised by 50–75 m, which is the baroclinic response to the gyre’s
 406 spin-down (Fig. 5d; note that this is the same dynamical process as reported by Dotto
 407 et al. (2022)). This shoaling of the isotherms occurs over a large portion of the eastern
 408 Amundsen embayment that includes TIS, CIS and DIS, and it directly impacts their ther-
 409 mal forcing given the quasi-linear thermal stratification of the region (see §2.5). Between
 410 experiments 2022noFastI and 2022, the basal melt of CIS increases by 10%, exemplify-
 411 ing the remote impact of the gyre’s spin-down on the thermal forcing (Table 1). The shoal-
 412 ing of the isotherms impacts TIS the most (Fig. 5d) with a corresponding increase of 17%
 413 in its basal melt (Table 1).

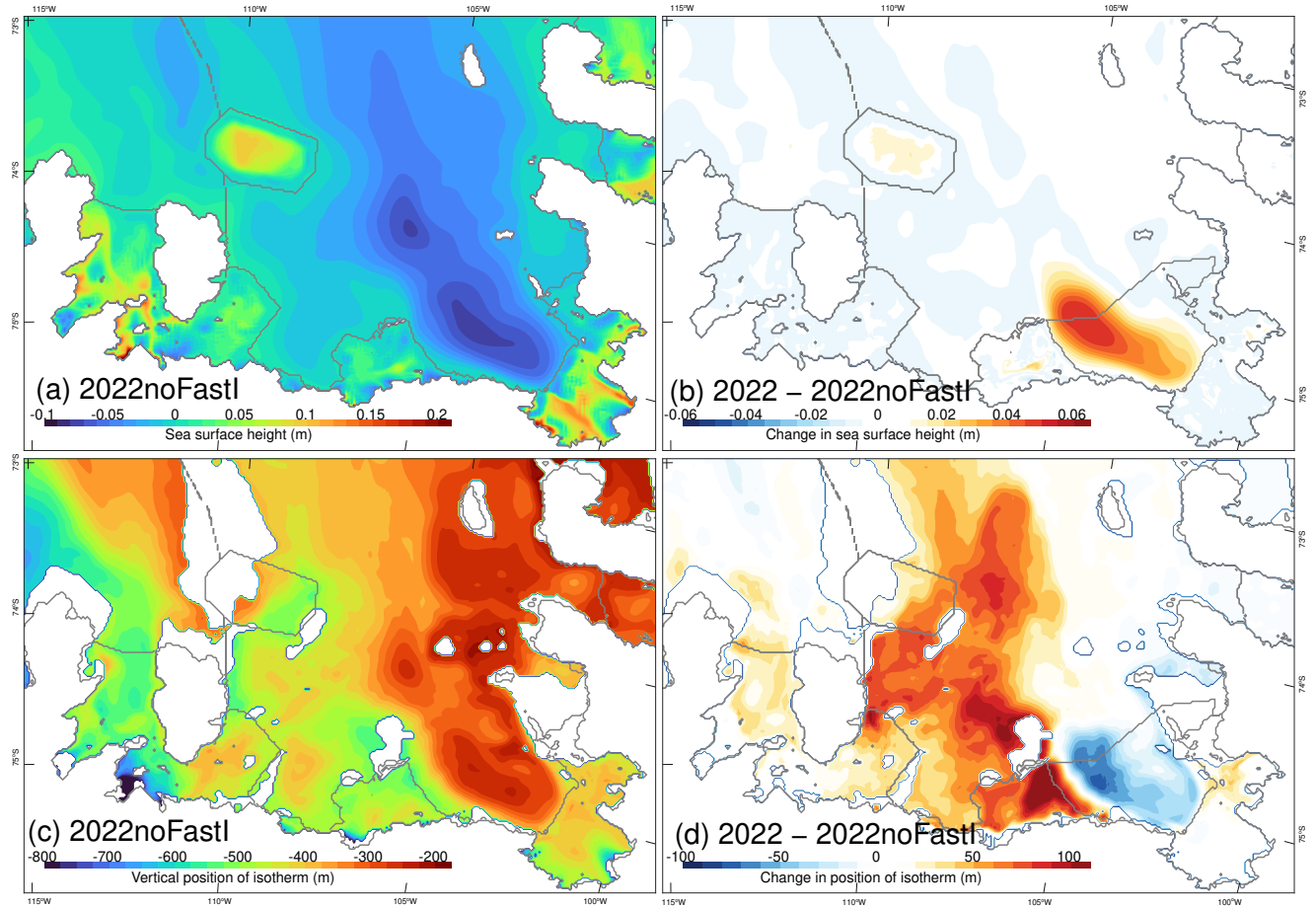


Figure 5. Impact of the fast-ice cover on the circulation and hydrography. (a) Sea surface height of experiment 2022noFastI. (b) Change in sea surface height due to the fast-ice cover. (c) Vertical position of the 0°C isotherm in experiment 2022noFastI (values increase upward; this particular isotherm is representative of the thermocline). White areas correspond to land and/or isotherm outcrops. (d) Change in the position of the isotherm due to the fast-ice cover. All fields are averaged over year 2011.

3.3 Sea ice growth in polynyas after changes in icescape

Yearly changes in the Amundsen icescape have the potential to modify surface heat exchanges and sea ice growth substantially. This is examined by horizontally averaging the ocean surface fluxes over the central (110–120°W, 72–75°S, area of 8.78×10^4 km²) and eastern (100–110°W, 72–75°S, area of 9.23×10^4 km²) Amundsen continental shelf. These two areas are representative of the Amundsen and Pine Island polynyas (respectively). The averaging assumes a flux of zero under ice shelves, icebergs, and PIS’ fast-ice, to specifically reflect exchanges between ocean and atmosphere/sea-ice. Note that in general, the wintertime variability of the surface heat flux mostly reflects fluctuations in the polynyas’ extent and meteorology rather than surface oceanic temperatures (which are always confined to a narrow range of a few °C).

Experiment 2011 exhibits oceanic warming in January, neutral values in December/February, and cooling over the rest of the year (Fig. 6a,b). Sea ice melt is concentrated in January–February (i.e. a few months following the opening of the polynyas) while sea ice growth can occur anywhere from March to November (Fig. 6c,d). Only minor differences are apparent between experiments 2011 and 2022, which indicates that regionally-averaged fluxes are primarily set by the meteorology (which is the same in both experiments) and that the collapse of the TGT has a minor impact on sea ice growth in the polynyas (Fig. 6; growth is typically concentrated along the eastern edge of the two regions). Similarly, temperature conditions in the central Amundsen are largely unaffected by icescape changes taking place east of the BRIC (compare experiments 2011 and 2022 in Fig. 6e). In the eastern Amundsen, however, a small +0.1°C warming is apparent in the bottom layer between experiments 2011 and 2022 (Fig. 6f) primarily due to the fast-ice near PIS (§3.2).

The removal of the BRIC (experiment 2022noBerg) has a major impact on sea ice distributions and in turn the surfaces fluxes. Without this barrier, sea ice growth in the central region entirely depends on winds having a southerly component (i.e. directed offshore) to generate open water and large sea ice growth (compare Figs. 3, 7 and S10). Sea ice growth in the central region thus decreases by 53% in experiment 2022noBerg and the surface heat flux decreases by 27% (values averaged over year 2011; Fig. 6). Turning to the eastern region, the absence of the BRIC allows newly-produced sea ice to be continuously evacuated by the dominant easterly winds. Sea ice growth in this area thus increases by 30% between experiments 2011 and 2022noBerg, but this increase offsets only ~half of the decrease occurring in the central region. (Similar outcomes were reported by Nakayama et al. (2014); Bett et al. (2020) for a comparable experiment.) Overall, experiment 2022noBerg suggests that the disappearance of the BRIC would change the spatial distribution of sea ice production and decrease its magnitude substantially over the Amundsen shelf as a whole. On the other hand, these substantial changes in sea ice do not affect the heat supply appreciably (§3.1, Table 1). The largest impact on oceanic temperatures is apparent in the central Amundsen where the signature of the cold winter mixed layer becomes subdued (Fig. 6e) following the reduction in polynya extent.

The same analyses conducted with the meteorology and hydrography of 2015 (cool conditions; §2.3) lead to the same outcomes (Fig. S8). Sea ice growth in the central region decreases by 58% in experiment 2022noBerg_cold and the surface heat flux decreases by 24% (values averaged over year 2015). In the eastern region, sea ice growth increases by 35% between experiments 2011_cold and 2022noBerg_cold. Overall, the impact of icescape changes on polynya fluxes appears to be robust across meteorologic and hydrographic conditions.

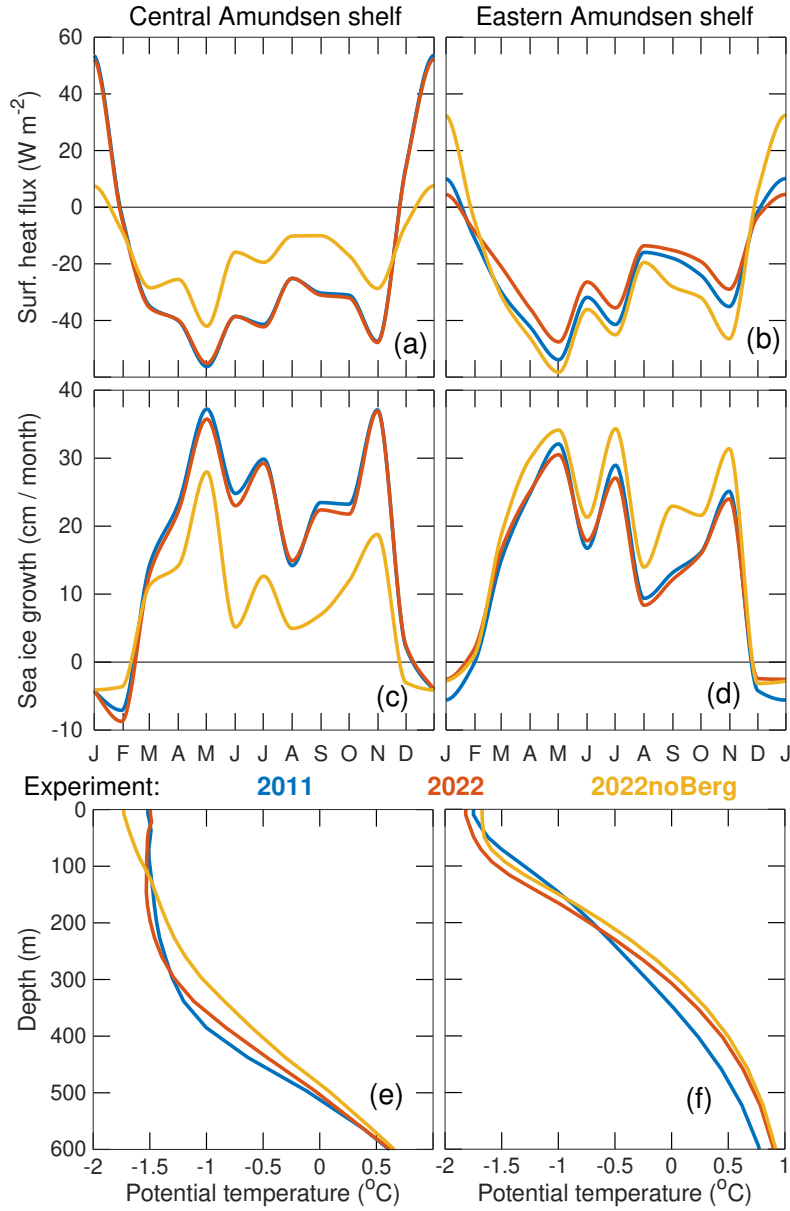


Figure 6. Surface fluxes horizontally-averaged over the central/eastern Amundsen continental shelf and oceanic temperature profiles (year 2011). The central and eastern regions are defined as $110\text{--}120^\circ\text{W}, 72\text{--}75^\circ\text{S}$ and $100\text{--}110^\circ\text{W}, 72\text{--}75^\circ\text{S}$ (respectively) and loosely correspond to the Amundsen Sea Polynya and Pine Island Polynya. In (a,b), the heat flux is defined positive if warming the ocean. In (c,d), negative sea ice growth represents sea ice melt. (e,f) Temperature profiles are from locations representative of the two polynyas ($73^\circ\text{S}, 115^\circ\text{W}$ and $74.25^\circ\text{S}, 105^\circ\text{W}$, respectively) and averaged over year 2011.

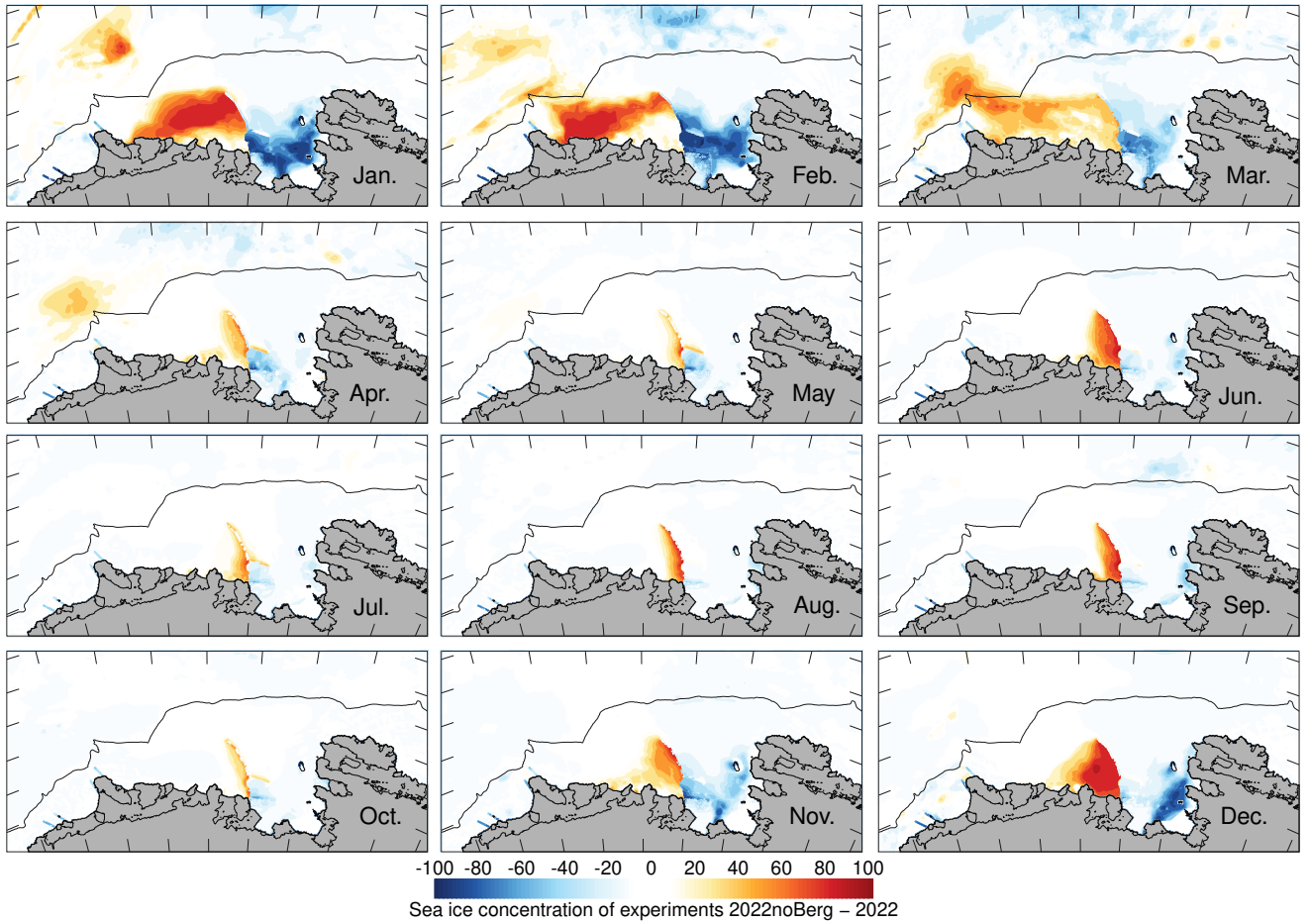


Figure 7. Differences in modeled sea ice concentration between experiments 2022noBerg and 2022. All fields are monthly averages centered around the first day of the month (1 Jan. 2011 to 1 Dec. 2011). The black horizontal line depicts the shelf break. See Fig. S10 for the absolute sea ice concentrations of experiment 2022noBerg.

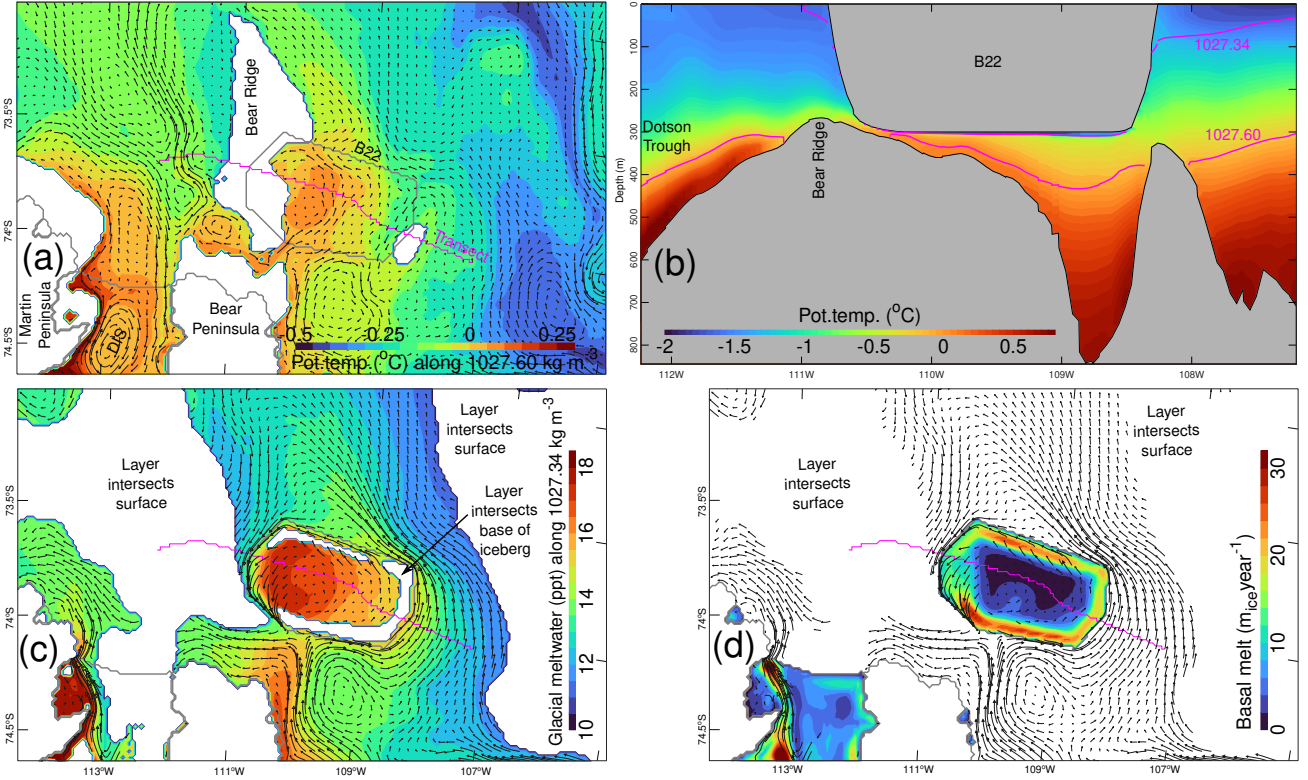


Figure 8. Physical conditions around tabular iceberg B22 in experiment 2022. (a) Potential temperature and oceanic flow for a layer representative of mCDW underneath B22 ($1027.60 \text{ kg m}^{-3}$, $\sim 350 \text{ m}$ depth). The magenta line represents the transect of figure b. (b) Transect along the length of B22 with potential temperature and the position of layers 1027.34 and $1027.60 \text{ kg m}^{-3}$. (c) Circulation and glacial meltwater for a layer grazing the bottom of B22 ($1027.34 \text{ kg m}^{-3}$). (d) Basal melt rate and circulation along $1027.34 \text{ kg m}^{-3}$. All fields are averaged over year 2011.

463

3.4 Circulation and melt under a tabular iceberg (B22)

464

465

466

467

468

469

470

471

472

473

474

475

The circulation of oceanic heat around tabular iceberg B22 is examined in the icescape configuration of 2022 (i.e., when B22 is independent from the TGT). Given the weak ambient stratification (Rossby radius of $\sim 4.4 \text{ km}$) and the assumed iceberg keel of 300 m (see §2), and based on the two-layer model of Ou (1991), one expects partial blocking in the top layer and a bottom layer that is either not blocked or only partially blocked. The 3D model of this study suggests that mCDW flows northward along the eastern edge of Bear Peninsula and then crosses iceberg B22 from one side to the other while supplying it with warm water ($\sim 0.05^\circ\text{C}$; Fig. 8a,b). Such an unimpeded flow in the bottom layer is confirmed by contours of potential vorticity $f/h = f(-\partial\rho_{pot}/\partial z)/\Delta\rho$ (with f the Coriolis parameter, h the layer's thickness, ρ_{pot} seawater potential density, z pointing upward, and $\Delta\rho$ an arbitrary constant) being continuous in and out of B22 for a layer representative of mCDW ($1027.60 \text{ kg m}^{-3}$; not shown).

476

477

478

479

The situation reverses in the shallower layers where blocking becomes more apparent. In a layer representative of conditions just below B22 ($1027.34 \text{ kg m}^{-3}$, Fig. 8b), the flow upstream of B22 splits upon reaching the iceberg and is nearly everywhere tangential to B22's outline (Fig. 8c). In the iceberg's inner region, the flow is dominated by

an anticyclonic (i.e., counterclockwise) circulation that is most vigorous at the edges of B22. It is unclear to what extent the anticyclonic cell reflects a Taylor column or a melt-driven circulation, and it is worth pointing out that the edge of the iceberg is where the model dynamics are most likely to be affected by the vertical coordinate (see §2.1 and the Discussion). The melting rates under B22 reach up to 25 m of ice per year and are generally concentrated along the edges of the iceberg where flow velocities are the strongest (Fig. 8d). Glacial meltwater concentrations (estimated from modeled salinity and potential temperature following Jenkins et al. (2018)) thus reach up to 17 ppt in the iceberg’s inner region (Fig. 8c). In spite of the anticyclonic circulation, some of the meltwater appears to escape B22 at its southwest corner and to ultimately join the meltwater outflow from CIS (Fig. 8c). Overall, the horizontally-integrated melt of B22 amounts to 30.7 Gt yr⁻¹ on average over year 2011.

4 Discussion

The key outcome of the study (based on the finite number of experiments conducted) is that changes in the coastal icescape are unlikely to reverse or even mitigate the high ice shelf melting rates of the Amundsen Sea. Basal melt rates remain high in all the experiments and even increase after the formation of a fast-ice cover next to PIS (§3.1–3.2). Although lower melt rates occur in the 2011 icescape configuration (Table 1), the changes between the 2011/2022 configurations are smaller than those seen in multi-decadal simulations with time-invariant icescapes (Naughten et al., 2022; St-Laurent et al., 2022) or in interannual field campaigns (Jenkins et al., 2018). The same conclusion is obtained in two different time periods (2010–2011 and 2014–2015) with substantially different hydrographic conditions and different meteorology. What becomes apparent from §3.1 is that ice shelves such as TIS or CIS have multiple viable pathways for heat supply. Recent fieldwork supports this view that ice shelves may have multiple sources of warm deep water (see Fig. 6 of Wählin et al. (2021) in the case of TIS, and Girton et al. (2019) for CIS). The available data also do not refute the possibility that the sources’ relative importance could shift over the years to accommodate major changes in icescape (such as the presence/absence of the TGT; §3.1), in such a way that the high melting rates we currently experience (Rignot et al., 2019) can continue unabated.

An icescape modification of a different type was considered by Bett et al. (2020) whereas a surface freshwater flux is prescribed near the coast to mimic iceberg melt. As in the present study, this addition did not reverse the high ice shelf melting rates, but actually increased bottom water temperatures on the shelf. Bett et al. (2020) attributed this result to weaker wintertime oceanic cooling in presence of the stabilizing surface buoyancy input. Overall, these results do not support the idea that changes in the Amundsen’s icebergs/fast-ice would slow down the melt of ice shelves. Reversing the current high melting rates appears to require a change in the regional wind regime in order to, e.g., slow down the onshelf flux of mCDW (e.g., Silvano et al., 2022; Thoma et al., 2008), or enhance wintertime oceanic cooling upstream of ice shelves (Bett et al., 2020; Webber et al., 2017). This being said, the present study does not cover all the possible types of icescape changes. Other perturbations that took place in recent years include a retreat of the ice front of PIS (see Yoon et al., 2022; Bradley et al., 2022, 2023) and changes in the grounding zone of TIS (see Milillo et al., 2019; Holland et al., 2023). Future extreme icescape changes of such types (which were not explored in this study) could possibly lead to a reduction in ice shelf basal melt rates.

The study of Dotto et al. (2022) provides observational support for the substantial increase (+17%) in TIS’ basal melt between experiments 2022noFastI and 2022 (§3.2). However, the present study suggests that the footprint of the gyre extends beyond TIS, and reaches as far as CIS and DIS (§3.2). This model result, along with the substantial throughflow between DIS and CIS (see §3.1, and the observations of Girton et al. (2019)) overall suggest that ice shelf cavities influence each other to a certain extent. Such re-

532 mote connections can only be captured in regional models or with simultaneous mea-
 533 surements across regions of the Amundsen Sea (e.g., Azaneu et al., 2023).

534 The unimpeded flow of mCDW under B22 (§3.4) suggests that a surface obsta-
 535 cle is less constraining for mCDW than a bottom obstacle such as Bear Ridge (that di-
 536 vides mCDW into two geographical regions; see Fig. 1a of Dutrieux et al. (2014)). It also
 537 suggests a continuous supply of heat to the iceberg while it remains within the limits of
 538 the Amundsen continental shelf. Although the freshwater input associated with iceberg
 539 melt in the Amundsen remains uncertain and a topic of active research (e.g., Tournadre
 540 et al., 2016), the 30.7 Gt yr⁻¹ contribution of B22 (§3.4) amounts to as much as one third
 541 of that of TIS even though the latter exhibits basal melt rates > 100 m_{ice} yr⁻¹ near the
 542 grounding zone (Fig. S6). The model may exaggerate the melt of B22 since the highest
 543 rates occur at the transition between the horizontal base and the vertical walls of the
 544 iceberg (Fig. 8) which only approximates the true geometry (see §2.1). The basal melt
 545 rates of iceberg B22 and the behavior of the shallow layer (1027.34 kg m⁻³, Fig. 8) are
 546 therefore uncertain. For comparisons, Jenkins (1999) suggests heat fluxes of 150–300 W m⁻²
 547 (equivalent to 15–30 m_{ice} yr⁻¹) under icebergs which would correspond to the high end
 548 of Fig. 8d. Iceberg models also indicate that on the scale of the Southern Ocean, wave
 549 erosion (not represented here) is a larger mass sink than basal melt, but at the same time,
 550 the influence of the former decreases in high sea ice conditions typical of continental shelves
 551 (see Martin & Adcroft, 2010). With a basal melt of 30.7 Gt yr⁻¹, B22 by itself would
 552 be contributing to as much as 4% of the global iceberg basal melt estimated at ~ 700 Gt yr⁻¹
 553 by Martin and Adcroft (2010). On the other hand, the large area of B22 is a rarity in
 554 Antarctic iceberg size distributions (Tournadre et al., 2016) and its ultimate fate was to
 555 drift offshore rather than to melt locally. Overall, the magnitude of the freshwater input
 556 from icebergs in the Amundsen Sea remains a substantial uncertainty.

557 Open Research Section

558 The model results supporting the conclusions are publicly available at:
 559 <https://www.dropbox.com/sh/t80rb14babrx9dm/AAAWRNuIfx0sAE1SWa1bowZ8a?dl=0>
 560 and will be migrated to an official repository (e.g., SEANOE, Zenodo) once the manuscript
 561 is accepted. The ROMS computer code and input files are publicly available from St-
 562 Laurent (2023). ERA5 reanalyses were obtained from Hersbach et al. (2023). Hydrographic
 563 observations from ASPIRE were obtained from P. Yager and Sherrell (2019) and hydro-
 564 graphic observations from cruise NBP09-01 were obtained from Boyer et al. (2018).

565 Acknowledgments

566 This research was supported by NASA (award 80NSSC21K0746, Antarctic sea ice, fast
 567 ice and icebergs: Modulators of ocean-ice shelf interactions (AMICUS)) and by NSF (col-
 568 laborative awards 1941292, 1941327). We thank M.S.Dinniman (Old Dominion Univer-
 569 sity) for providing 5 km-resolution circumpolar model outputs for lateral oceanic bound-
 570 ary conditions as well as for helpful advice. The authors acknowledge William & Mary
 571 Research Computing (<https://www.wm.edu/it/rc>) for providing computational resources
 572 and/or technical support that have contributed to the results reported within this study.
 573 We thank the referees for their careful reading of the manuscript and for providing help-
 574 ful and thoughtful comments.

575 References

576 Azaneu, M., Webber, B., Heywood, K. J., Assmann, K. M., Dotto, T. S., & Abra-
 577 hamsen, E. P. (2023). Influence of shelf break processes on the transport of
 578 warm waters onto the eastern Amundsen Sea continental shelf. *J. Geophys.*
 579 *Res. Oceans*, 128(e2022JC019535). doi: 10.1029/2022JC019535

- 580 Bett, D. T., Holland, P. R., Garabato, A. C. N., Jenkins, A., Dutrieux, P., Kimura,
581 S., & Fleming, A. (2020). The impact of the Amundsen Sea freshwater balance
582 on ocean melting of the west Antarctic ice sheet. *J. Geophys. Res. Oceans*,
583 *125*(e2020JC016305). doi: 10.1029/2020JC016305
- 584 Boyer, T. P., Baranova, O. K., Coleman, C., Garcia, H. E., Grodsky, A., Locarnini,
585 R. A., ... Zweng, M. M. (2018). *World Ocean Database 2018* [Dataset]. A. V.
586 Mishonov, Technical Ed., NOAA Atlas NESDIS 87, Subset: cruise NBP09-01
587 Jan.–Feb. 2009 72–90°S, 100–110°W, accessed 2023-12-08. Retrieved from
588 [https://www.ncei.noaa.gov/access/world-ocean-database-select/
589 dbsearch.html](https://www.ncei.noaa.gov/access/world-ocean-database-select/dbsearch.html)
- 590 Bradley, A. T., Bett, D. T., Dutrieux, P., De Rydt, J., & Holland, P. R. (2022). The
591 influence of Pine Island ice shelf calving on basal melting. *J. Geophys. Res.*
592 *Oceans*, *127*(e2022JC018621). doi: 10.1029/2022JC018621
- 593 Bradley, A. T., De Rydt, J., Bett, D. T., Dutrieux, P., & Holland, P. R. (2023). The
594 ice dynamic and melting response of Pine Island ice shelf to calving. *Annals of*
595 *Glaciology*, *63*(87-89), 111-115. doi: 10.1017/aog.2023.24
- 596 Budgell, W. P. (2005). Numerical simulation of ice-ocean variability in the Barents
597 Sea region: Towards dynamical downscaling. *Ocean Dyn.*, *55*, 370-387. doi: 10
598 .1007/s10236-005-0008-3
- 599 Comiso, J. C. (2017). *Bootstrap sea ice concentrations from Nimbus-7 SMMR and*
600 *DMSP SSM/I-SSMIS, version 3 (2010–2011 used)*. Boulder, Colorado USA.
601 NASA National Snow and Ice Data Center Distributed Active Archive Center,
602 accessed 11 February 2022. doi: 10.5067/7Q8HCCWS4I0R
- 603 Cougnon, E. A., Galton-Fenzi, B. K., Fraser, A. D., & Hunter, J. R. (2017). Re-
604 gional changes in icescape impact shelf circulation and basal melting. *Geophys-*
605 *ical Research Letters*, *44*, 11519-11,527. doi: 10.1002/2017GL074943
- 606 De Rydt, J., Holland, P. R., Dutrieux, P., & Jenkins, A. (2014). Geometric and
607 oceanographic controls on melting beneath Pine Island Glacier. *J. Geophys.*
608 *Res. Oceans*, *119*, 2420-2438. doi: 10.1002/2013JC009513
- 609 Dinniman, M. S., Klinck, J. M., & Smith Jr., W. O. (2011). A model study of Cir-
610 cumpolar Deep Water on the west Antarctic Peninsula and Ross Sea continen-
611 tal shelves. *Deep Sea Res. II*, *58*, 1508-1523. doi: 10.1016/j.dsr2.2010.11.013
- 612 Dinniman, M. S., St-Laurent, P., Arrigo, K. R., Hofmann, E. E., & van Dijken,
613 G. L. (2020). Analysis of iron sources in Antarctic continental shelf waters. *J.*
614 *Geophys. Res.: Oceans*, *125*(e2019JC015736). doi: 10.1029/2019JC015736
- 615 Dorschel, B., Hehemann, L., Viquerat, S., Warnke, F., Dretter, S., Tenberge, Y. S.,
616 ... Arndt, J. E. (2022). The International Bathymetric Chart of the Southern
617 Ocean version 2. *Scientific Data*, *9*. doi: 10.1038/s41597-022-01366-7
- 618 Dotto, T. S., Heywood, K. J., Hall, R. A., Scambos, T. A., Zheng, Y., Nakayama,
619 Y., ... Pettit, E. (2022). Ocean variability beneath Thwaites eastern ice
620 shelf driven by the Pine Island bay gyre strength. *Nature Communications*,
621 *13*(7840). doi: 10.1038/s41467-022-35499-5
- 622 Dutrieux, P., De Rydt, J., Jenkins, A., Holland, P. R., Ha, H. K., Lee, S. H., ...
623 Schroder, M. (2014). Strong sensitivity of Pine Island ice-shelf melting to
624 climatic variability. *Science*, *343*(174), 174-178. doi: 10.1126/science.1244341
- 625 Girton, J. B., Christianson, K., Dunlap, J., Dutrieux, P., Gobat, J., Lee, C.,
626 & Rainville, L. (2019). Buoyancy-adjusting profiling floats for explo-
627 ration of heat transport, melt rates, and mixing in the ocean cavities un-
628 der floating ice shelves. *Oceans 2019 MTS/IEEE Seattle*, 1–6. doi:
629 10.23919/OCEANS40490.2019.8962744
- 630 Gwyther, D. E., Kusahara, K., Asay-Davis, X. S., Dinniman, M. S., & Galton-
631 Fenzi, B. K. (2020). Vertical processes and resolution impact ice shelf
632 basal melting: A multi-model study. *Ocean Modelling*, *147*. doi: 10.1016/
633 j.ocemod.2020.101569
- 634 Hersbach, H., Bell, B., Berrisford, P., Biavati, G., Horanyi, A., Sabater, J. M., ...

- 635 Thepaut, J. N. (2023). *ERA5 hourly data on single levels from 1940 to*
636 *present* [Dataset]. Copernicus Climate Change Service (C3S) Climate Data
637 Store (CDS). Retrieved from <https://cds.climate.copernicus.eu> doi:
638 10.24381/cds.adbb2d47
- 639 Hersbach, H., Bell, B., Berrisford, P., Hirahara, S., Horányi, A., Muñoz-Sabater, J.,
640 ... Thépaut, J.-N. (2020). The ERA5 global reanalysis. *Q J R Meteorol Soc.*,
641 *146*, 1999-2049. doi: 10.1002/qj.3803
- 642 Holland, P. R., Bevan, S. L., & Luckman, A. J. (2023). Strong ocean melting
643 feedback during the recent retreat of Thwaites glacier. *Geophys. Res. Lett.*,
644 *50*(e2023GL103088). doi: 10.1029/2023GL103088
- 645 Jacobs, S., Jenkins, A., Hellmer, H., Giulivi, C., Nitsche, F., Huber, B., & Guerrero,
646 R. (2012). The Amundsen Sea and the Antarctic Ice Sheet. *Oceanography*,
647 *25*(3), 154-163. doi: 10.5670/oceanog.2012.90
- 648 Jenkins, A. (1999). The impact of melting ice on ocean waters. *J. Phys. Oceanogr.*,
649 *29*, 2370-2381.
- 650 Jenkins, A., Shoosmith, D., Dutrieux, P., Jacobs, S., Kim, T. W., Lee, S. H., ...
651 Stammerjohn, S. (2018). West Antarctic Ice Sheet retreat in the Amundsen
652 Sea driven by decadal oceanic variability. *Nature Geoscience*, *11*, 733-738. doi:
653 10.1038/s41561-018-0207-4
- 654 Jordan, T. A., Porter, D., Tinto, K., Millan, R., Muto, A., Hogan, K., ... Paden,
655 J. D. (2020). New gravity-derived bathymetry for the Thwaites, Crosson, and
656 Dotson ice shelves revealing two ice shelf populations. *The Cryosphere*, *14*.
657 doi: 10.5194/tc-14-2869-2020
- 658 Joughin, I., Shapero, D., Dutrieux, P., & Smith, B. (2021). Ocean-induced melt
659 volume directly paces ice loss from Pine Island Glacier. *Science Advances*,
660 *7*(eabi5738). doi: 10.1126/sciadv.abi5738
- 661 Jourdain, N. C., Mathiot, P., Merino, N., Durand, G., Sommer, J. L., Spence, P., ...
662 Madec, G. (2017). Ocean circulation and sea-ice thinning induced by melting
663 ice shelves in the Amundsen Sea. *J. Geophys. Res. Oceans*, *122*, 2550-2573.
664 doi: 10.1002/2016JC012509
- 665 Jourdain, N. C., Molines, J. M., Sommer, J. L., Mathiot, P., Chanut, J., de
666 Lavergne, C., & Madec, G. (2019). Simulating or prescribing the influence
667 of tides on the Amundsen Sea ice shelves. *Ocean Modelling*, *133*, 44-55. doi:
668 10.1016/j.ocemod.2018.11.001
- 669 Kim, T. W., Yang, H. W., Dutrieux, P., Wählin, A. K., Jenkins, A., Kim, Y. G.,
670 ... Cho, Y. K. (2021). Interannual variation of modified Circumpolar Deep
671 Water in the Dotson-Getz Trough, west Antarctica. *J. Geophys. Res.: Oceans*,
672 *126*(e2021JC017491). doi: 10.1029/2021JC017491
- 673 Macdonald, G. J., Ackley, S. F., Mestas-Nunez, A. M., & Blanco-Cabanillas, A.
674 (2023). Evolution of the dynamics, area, and ice production of the Amund-
675 sen Sea Polynya, Antarctica, 2016–2021. *The Cryosphere*, *17*, 457-476. doi:
676 10.5194/tc-17-457-2023
- 677 MacGregor, J. A., Catania, G. A., Markowski, M. S., & Andrews, A. G. (2012).
678 Widespread rifting and retreat of ice-shelf margins in the eastern Amundsen
679 Sea Embayment between 1972 and 2011. *Journal of Glaciology*, *58*(209). doi:
680 10.3189/2012JoG11J262
- 681 Martin, T., & Adcroft, A. (2010). Parameterizing the fresh-water flux from land
682 ice to ocean with interactive icebergs in a coupled climate model. *Ocean Mod-*
683 *elling*, *34*, 111-124. doi: 10.1016/j.ocemod.2010.05.001
- 684 Mazur, A. K., Wählin, A. K., & Kalen, O. (2019). The life cycle of small- to
685 medium-sized icebergs in the Amundsen sea embayment. *Polar Research*,
686 *38*(3313). doi: 10.33265/polar.v38.3313
- 687 Miles, B. W. J., Stokes, C. R., Jenkins, A., Jordan, J. R., Jamieson, S. S. R., &
688 Gudmundsson, G. H. (2020). Intermittent structural weakening and acceler-
689 ation of the Thwaites Glacier Tongue between 2000 and 2018. *J. Glaciology*,

- 690 66(257), 485-495. doi: 10.1017/jog.2020.20
- 691 Milillo, P., Rignot, E., Rizzoli, P., Scheuchl, B., Mouginot, J., Bueso-Bello,
692 J., & Prats-Iraola, P. (2019). Heterogeneous retreat and ice melt of
693 Thwaites Glacier, west Antarctica. *Science Advances*, 5(1). doi: 10.1126/
694 sciadv.aau3433
- 695 Morlighem, M. (2020). *MEaSUREs BedMachine Antarctica, version 2020-10-*
696 *08, accessed 2020-10-08*. Boulder, Colorado USA. NASA National Snow
697 and Ice Data Center Distributed Active Archive Center. doi: 10.5067/
698 E1QL9HFQ7A8M
- 699 Nakayama, Y., Timmermann, R., Schroder, M., & Hellmer, H. H. (2014).
700 On the difficulty of modeling Circumpolar Deep Water intrusions onto
701 the Amundsen Sea continental shelf. *Ocean Modelling*, 84, 26-34. doi:
702 10.1016/j.ocemod.2014.09.007
- 703 Naughten, K. A., Holland, P. R., Dutrieux, P., Bett, D. T., & Jenkins, A.
704 (2022). Simulated twentieth-century ocean warming in the Amundsen
705 Sea, west Antarctica. *Geophys. Res. Lett.*, 49(e2021GL094566). doi:
706 10.1029/2021GL094566
- 707 Ou, H. W. (1991). Some effects of a seamount on oceanic flows. *J. Phys. Oceanogr.*,
708 21, 1835-1845.
- 709 Padman, L., Fricker, H. A., Coleman, R., Howard, S., & Erofeeva, L. (2002). A new
710 tide model for the Antarctic ice shelves and seas. *Annals of Glaciology*, 34.
- 711 Pritchard, H. D., Ligtenberg, S. R., Fricker, H. A., Vaughan, D. G., van den Broeke,
712 M. R., & Padman, L. (2012). Antarctic ice-sheet loss driven by basal melting
713 of ice shelves. *Nature*, 484, 502-505. doi: 10.1038/nature10968
- 714 Randall-Goodwin, E., Meredith, M. P., Jenkins, A., Yager, P. L., Sherrell, R. M.,
715 Abrahamsen, E. P., ... Stammerjohn, S. E. (2015). Freshwater distributions
716 and water mass structure in the Amundsen Sea Polynya region, Antarctica.
717 *Elem. Sci. Anthropocene*, 3(65). doi: 10.12952/journal.elementa.000065
- 718 Rignot, E., Jacobs, S., Mouginot, J., & Scheuchl, B. (2013). Ice-shelf melting around
719 Antarctica. *Science*, 341, 266-270. doi: 10.1126/science.1235798
- 720 Rignot, E., Mouginot, J., Scheuchl, B., van der Broeke, M., van Wessem, M. J.,
721 & Morlighem, M. (2019). Four decades of Antarctic ice sheet mass bal-
722 ance from 1979–2017. *Proc. Natl. Acad. Sci.*, 116(4), 1095-1103. doi:
723 10.1073/pnas.1812883116
- 724 Scambos, T., Wallin, B., & Bohlander, J. (2022). *Images of Antarctic ice shelves,*
725 *version 2, accessed 16 february 2023, subset 2001–2022 used*. Boulder, Col-
726 orado USA. NASA National Snow and Ice Data Center Distributed Active
727 Archive Center. doi: 10.5067/W87VCY3CW0MJ
- 728 Shchepetkin, A. F., & McWilliams, J. C. (2003). A method for computing hori-
729 zontal pressure-gradient force in an oceanic model with a nonaligned vertical
730 coordinate. *J. Geophys. Res.: Oceans*, 108(C3). doi: 10.1029/2001JC001047
- 731 Shchepetkin, A. F., & McWilliams, J. C. (2005). The Regional Oceanic Modeling
732 System (ROMS): A split-explicit, free-surface, topography-following-coordinate
733 oceanic model. *Ocean Model.*, 9, 347-404. doi: 10.1016/j.ocemod.2004.08.002
- 734 Silvano, A., Holland, P. R., Naughten, K. A., Dragomir, O., Dutrieux, P., Jenkins,
735 A., ... Garabato, A. C. N. (2022). Baroclinic ocean response to climate
736 forcing regulates decadal variability of ice-shelf melting in the Amundsen Sea.
737 *Geophys. Res. Lett.*, 49(e2022GL100646). doi: 10.1029/2022GL100646
- 738 Stammerjohn, S. E., Maksym, T., Massom, R. A., Lowry, K. E., Arrigo, K. R.,
739 Yuan, X., ... Yager, P. L. (2015). Seasonal sea ice changes in the Amundsen
740 Sea, Antarctica, over the period of 1979–2014. *Elem. Sci. Anthropocene*, 3(55).
741 doi: 10.12952/journal.elementa.000055
- 742 St-Laurent, P. (2023). *Dataset: A numerical simulation of the ocean, sea ice and ice*
743 *shelves in the Amundsen Sea (Antarctica) over the period 2006-2022 and its*
744 *associated code and input files (size 2.2 terabytes)* [Dataset]. William & Mary

- 745 Scholarworks. Retrieved from <https://doi.org/10.25773/bt54-sj65> doi:
746 10.25773/bt54-sj65
- 747 St-Laurent, P., Stammerjohn, S. E., Maksym, T., & Sherrell, R. M. (2022). *On*
748 *the relative importance of offshelf/onshelf drivers of variability in mCDW*
749 *inventory on the Amundsen shelf, Antarctica.* paper C15D-0621 pre-
750 sented at 2022 Fall Meeting, AGU, Chicago IL, 12–16 Dec. (available at
751 https://www.dropbox.com/s/dfxi1tiih7vvnv59/amundsen_fall_agu20221212.pdf?dl=0)
- 752
- 753 St-Laurent, P., Yager, P. L., Sherrell, R. M., Stammerjohn, S. E., & Dinniman,
754 M. S. (2017). Pathways and supply of dissolved iron in the Amund-
755 sen Sea (Antarctica). *J. Geophys. Res. Oceans*, *122*(9), 7135-7162. doi:
756 10.1002/2017jc013162
- 757 Thoma, M., Jenkins, A., Holland, D., & Jacobs, S. (2008). Modelling Circumpolar
758 Deep Water intrusions on the Amundsen Sea continental shelf, Antarctica.
759 *Geophys. Res. Lett.*, *35*(L18602). doi: 10.1029/2008GL034939
- 760 Thurnherr, A. M., Jacobs, S. S., Dutrieux, P., & Giulivi, C. F. (2014). Export and
761 circulation of ice cavity water in Pine Island Bay, West Antarctica. *J. Geophys.*
762 *Res.*, *119*, 1754-1764. doi: 10.1002/2013jc009307
- 763 Tournadre, J., Bouhier, N., Girard-Adhain, F., & Rémy, F. (2016). Antarctic ice-
764 bergs distributions 1992–2014. *J. Geophys. Res.: Oceans*, *121*, 327-349. doi: 10
765 .1002/2015JC011178
- 766 Wählin, A. K., Graham, A. G. C., Hogan, K. A., Queste, B. Y., Boehme, L., Larter,
767 R. D., . . . Heywood, K. J. (2021). Pathways and modification of warm wa-
768 ter flowing beneath Thwaites ice shelf, west Antarctica. *Science Advances*,
769 *7*(eabd7254). doi: 10.1126/sciadv.abd7254
- 770 Webber, B. G. M., Heywood, K. J., Stevens, D. P., Dutrieux, P., Abrahamsen,
771 E. P., Jenkins, A., . . . Kim, T. W. (2017). Mechanisms driving variability
772 in the ocean forcing of Pine Island Glacier. *Nat. Comm.*, *8*(14507). doi:
773 10.1038/ncomms14507
- 774 Yager, P., & Sherrell, R. (2019). *ASPIRE station data used to develop 1-D and*
775 *3-D numerical models from the Nathaniel B. Palmer in the Amundsen Sea*
776 *from 2010-12-14 through 2011-01-05* [Dataset]. Biological and Chemical
777 Oceanography Data Management Office (BCO-DMO). (Version 1) Version
778 Date 2019-04-17. doi: 10.1575/1912/bco-dmo.765081.1
- 779 Yager, P. L., Sherrell, R. M., Stammerjohn, S. E., Alderkamp, A. C., Schofield, O.,
780 Abrahamsen, E. P., . . . Wilson, S. (2012). ASPIRE: The Amundsen Sea
781 polynya international research expedition. *Oceanography*, *25*(3), 40-53. doi:
782 10.5670/oceanog.2012.73
- 783 Yager, P. L., Sherrell, R. M., Stammerjohn, S. E., Ducklow, H. W., Schofield, O. M.,
784 Ingall, E. D., . . . van Dijken, G. L. (2016). A carbon budget for the Amundsen
785 Sea Polynya, Antarctica: Estimating net community production and export in
786 a highly productive polar ecosystem. *Elem. Sci. Anthropocene*, *4*(140). doi:
787 10.12952/journal.elementa.000140
- 788 Yang, H. W., Kim, T. W., Dutrieux, P., Wählin, A. K., Jenkins, A., Ha, H. K.,
789 . . . Cho, Y. K. (2022). Seasonal variability of ocean circulation near the
790 Dotson ice shelf, Antarctica. *Nature Communications*, *13*(1138). doi:
791 10.1038/s41467-022-28751-5
- 792 Yoon, S. T., Lee, W. S., Nam, S., Lee, C. K., Yun, S., Heywood, K., . . . Bradley,
793 A. T. (2022). Ice front retreat reconfigures meltwater-driven gyres modulat-
794 ing ocean heat delivery to an Antarctic ice shelf. *Nature Communications*,
795 *13*(306). doi: 10.1038/s41467-022-27968-8
- 796 Zheng, Y., Stevens, D. P., Heywood, K. J., Webber, B. G. M., & Queste, B. Y.
797 (2022). Reversal of ocean gyres near ice shelves in the Amundsen Sea caused
798 by the interaction of sea ice and wind. *The Cryosphere*, *16*, 3005-3019. doi:
799 10.5194/tc-16-3005-2022